Angle dependence of dissociative tunneling ionization of NO in asymmetric two-color intense laser fields

Tomoyuki Endo [1,2] Hikaru Fujise [1] Hiroka Hasegawa,[1] Akitaka Matsuda [1] Mizuho Fushitani [1] Oleg I. Tolstikhin [3]
Toru Morishita,[4] and Akiyoshi Hishikawa [1,5,*]

[1]*Department of Chemistry, Graduate School of Science, Nagoya University, Furo-cho, Chikusa, Nagoya, Aichi 464-8602, Japan*

[2]*Kansai Photon Science Institute (KPSI), National Institutes for Quantum and Radiological Science and Technology (QST), 8-1-7 Umemidai, Kizugawa, Kyoto 619-0215, Japan*

[3]*Moscow Institute of Physics and Technology, Dolgoprudny 141700, Russia*

[4]*Institute for Advanced Science, The University of Electro-Communications, 1-5-1 Chofu-ga-oka, Chofu-shi, Tokyo 182-8585, Japan*

[5]*Research Center for Materials Science, Nagoya University, Furo-cho, Chikusa, Nagoya, Aichi 464-8602, Japan*

Dissociative tunneling ionization of nitric oxide (NO) in linearly polarized phase-locked two-color femtosecond intense laser fields (45 fs, $\lambda = 800$ and 400 nm, total field intensity $I = 1 \times 10^{14}$ W/cm^2) has been studied by three-dimensional ion momentum imaging. The N$^+$ fragment produced by the dissociative ionization, NO $\rightarrow$ NO$^+$ + e^- $\rightarrow$ N$^+$ + O + e^-, exhibits a butterflylike momentum distribution peaked at finite angles with respect to the laser polarization direction. In addition, a clear dependence on the relative phase between the two laser fields is observed, showing that the tunneling ionization occurs efficiently when the electric field points from N to O. For the highest kinetic energy component, the observed orientation dependence is well explained with theoretical calculations by the weak-field asymptotic theory for the 2π highest occupied molecular orbital (HOMO). On the other hand, the peak angle shifts toward the laser polarization direction as the kinetic energy decreases, indicating that pathways other than direct ionization from the HOMO contribute to the dissociative ionization.

I. INTRODUCTION

When molecules are exposed to intense laser fields, the electron binding potential is deformed to have a potential barrier. The electron ejection through the barrier, i.e., tunneling ionization, is one of the key processes of nonlinear molecular responses in intense laser fields, such as laser high-order harmonics generation, electron self-diffraction, and Coulomb explosion, which serve as spectroscopic tools for real-time probing of molecular dynamics (see, for example, [1,2] and references therein).

Since the tunneling ionization rate is sensitive to electron distributions at the asymptotic region, laser tunneling ionization can also provide a method to study the distribution of weakly bound electrons of atoms and molecules along the laser electric field. This unique feature can be applied to capture the angular distribution of electrons in molecules, in particular, in the highest occupied molecular orbitals (HOMOs). Experimentally, one can carry out such measurements either by varying the direction of the applied laser electric field with respect to spatially aligned or oriented molecules [3,4] or by measuring the molecular-frame photoelectron angular distributions (MFPADs) using circularly polarized laser fields [5–8]. Alternatively, one can utilize the spatial distribution of fragment ions produced by dissociative

ionization or Coulomb explosion after tunneling ionization [7,9–11]. Using these methods, experimental studies on the laser tunneling imaging of electron distributions were reported on various molecules in the ground state, such as H$_2$ (D$_2$) [5,8], N$_2$ [9], O$_2$ [9,12], CO [7,13], HCl [6], NO [11], CO$_2$ [10,14], and OCS [3,4]. Theoretical calculations have been carried out with different approaches, by tunneling ionization models [15–17] and the weak-field asymptotic theory (WFAT) [18,19], as well as time-dependent calculations based on single-active-electron approximation [20], the time-dependent density functional (TDDF) method [21], and the time-dependent Hartree-Fock (TDHF) method [22,23].

The experimental and theoretical studies triggered intensive discussions on the roles of various factors in the laser tunneling ionization, such as the permanent electric dipole [3,4], the contributions from next HOMOs [6,7,12,13], the molecular excitation [24], the interplay of coordinate- and momentum-space distributions [25], the field-induced distortion of MO [26,27], and the dynamic core polarization [22]. In particular, the angular dependence of tunneling ionization of CO has been a topic of hot debate [28] because of the discrepancies between the existing theories, predicting opposite electric-field directions to enhance the tunneling ionization.

Compared with CO, studies on another heterodiatomic molecule, NO, are rather sparse [11,29–32]. The electronic configuration in the ground state ($X\,^2\Pi$) is $1\sigma^2 2\sigma^2 3\sigma^2 4\sigma^2 5\sigma^2 1\pi^4 2\pi^1$. Unlike other molecules studied thus far, NO has one unpaired electron in the 2π HOMO. This
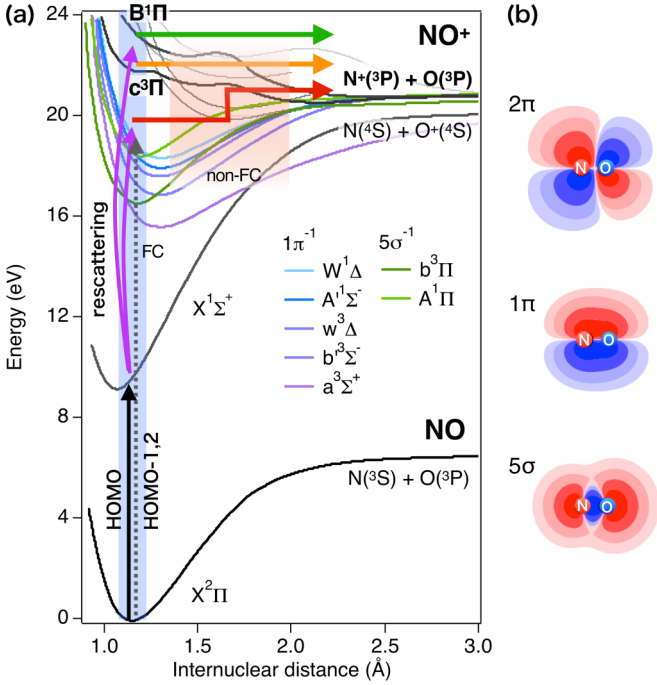
---

*hishi@chem.nagoya-u.ac.jp

FIG. 1. (a) Potential energy curves of selected electronic states of NO$^+$ [41,42] and NO. Possible dissociative ionization pathways are schematically shown, which involves electron rescattering excitation after the tunneling ionization to populate the dissociative $B\,^1\Pi$ and $c\,^3\Pi$ states in the Franck-Condon (FC) region, or photodissociation in the non-FC region, from the bound excited states of NO$^+$ (see text for details). (b) Relevant molecular orbitals of NO, 2π, 1π, and 5σ.

unique property should provide an alternative perspective to quantitatively understand the characteristics of molecular laser tunneling ionization. On the other hand, it is only very recently that the angular distributions of tunneling ionization yields were measured [11] by using the ion imaging of the dissociative ionization of NO (Fig. 1) in intense near-infrared (NIR) laser fields,

$$\mathrm{NO} \rightarrow \mathrm{N}^+ + \mathrm{O} + e^-, \tag{1}$$
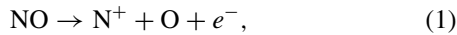
for the electronic ground ($X\,^2\Pi$) and excited ($A\,^2\Sigma^+$) states, with the latter being populated by transition from the 2π to the $3s\sigma$ orbital by UV photoabsorption. The obtained angular distributions are in good agreement with the theoretical predictions, demonstrating that the changes in the electron distribution upon photoexcitation can be captured by using the tunneling ionization [11]. However, it was not possible to study how the tunneling ionization is affected by the difference between the N and O sides in the amplitudes of the molecular orbitals (see Fig. 1) and the permanent dipole (or the effective ionization potential [3,4]), because the laser electric fields had symmetric amplitudes (see Sec. III A).

Here we employ phase-locked ω-2ω two-color laser fields [13,33–36]. The electric field may be expressed as

$$\boldsymbol{F}(t) = F(t)\boldsymbol{e}_z, \tag{2}$$

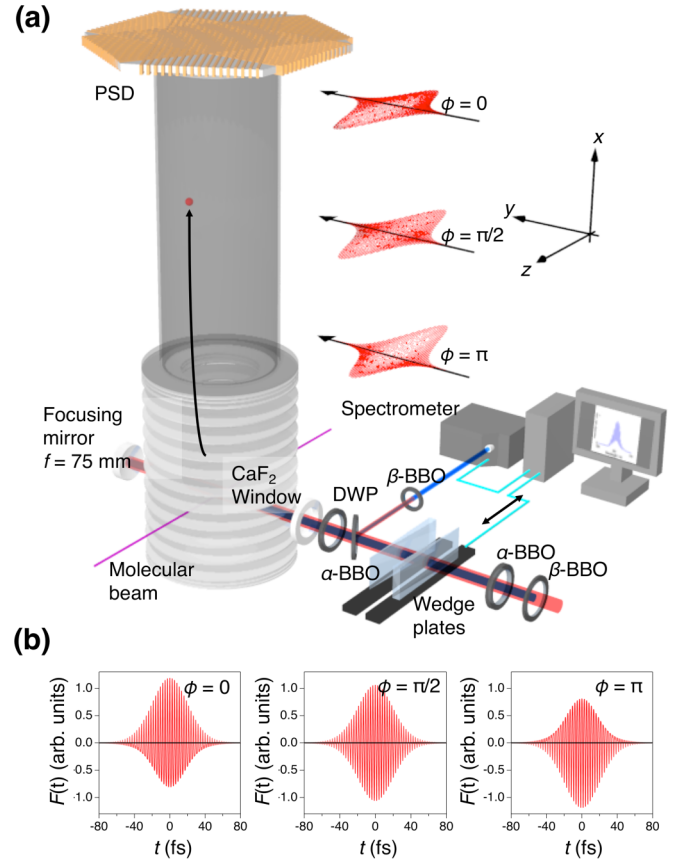$$F(t) = \bar{F}_\omega(t)\cos(\omega t) + \bar{F}_{2\omega}(t)\cos(2\omega t + \phi). \tag{3}$$

FIG. 2. (a) Schematic of the experimental setup. The fundamental femtosecond laser pulses (ω) (45 fs, 800 nm, 1 kHz) and the second harmonics (2ω) generated by a β-barium borate (BBO, type I) crystal are collinearly introduced to the three-dimensional ion momentum imaging spectrometer. The time delay between ω and 2ω pulses is controlled by birefringent α-BBO crystals and a pair of fused silica wedges. The relative phase is locked by a feedback loop utilizing the 2ω-2ω interference spectrum. The fragment ions produced from the interaction region are guided by a uniform electric field (61 V/cm) to reach a PSD through a field-free region. DWP: dual-wavelength wave plate; PSD: position-sensitive detector. (b) Temporal profiles of the two-color laser electric fields [Eq. (3)] for the relative phases of $\phi = 0$, $\pi/2$, and π, respectively, with the intensity ratio of $I_{2\omega}/I_\omega = 0.04$. The Gaussian functions are assumed for the envelopes, $\bar{F}_\omega(t)$ and $\bar{F}_{2\omega}(t)$. See Eq. (2) and inset of (a) for the definition of the field direction.

We choose the laser polarization to be along the z axis in the laboratory frame (see Fig. 2). In Eq. (3), $\bar{F}_\omega(t) > 0$ and $\bar{F}_{2\omega}(t) > 0$ are the temporal envelope functions of the fundamental and second-harmonic fields with carrier frequencies ω and 2ω, respectively, and ϕ is the relative phase between the two laser fields. Depending on the phase ϕ, the amplitude of the laser electric field becomes asymmetric as shown in Fig. 2(b).

In the present study, we discuss the angular dependence of tunneling ionization of NO in the two-color laser fields, by using momentum imaging of the N$^+$ fragment ions. We show that the angular distributions vary with the relative laser phase and the kinetic energy release of the dissociative ionization. The obtained results are compared with theoretical

calculation by the many-electron WFAT (ME-WFAT) for tunneling ionization [19] based on the Hartree-Fock (HF) approximation [37,38] to discuss key properties governing the laser tunneling ionization of NO such as the asymmetry of the molecular orbitals and the permanent electric dipole.

II. EXPERIMENT

The experimental setup (Fig. 2) is similar to that described previously [34,35], except that a stack of ion extraction electrodes is used to reduce distortions of the three-dimensional ion momentum images. The output of a Ti:sapphire laser amplification system (central wavelength 800 nm, repetition rate 1 kHz) was introduced to an inline two-color pulse generator, where the second harmonic was generated by a type-I β-barium borate (BBO) crystal. The time delay between the fundamental (ω) and second harmonic (2ω) pulses due to the group delay dispersion was compensated by birefringent (α-BBO) crystals. The relative phase between two laser pulses was monitored by the 2ω-2ω spectral interference and locked by a feedback loop using a pair of fused silica wedge plates mounted on a linear stage. The root mean square of the relative phase distribution was 2.5° (44 mrad). A true zero-order dual-wavelength wave plate ($\lambda/2$ for ω, λ for 2ω) was used to make the polarization directions parallel with each other. The absolute value of the relative phase in the interaction region was calibrated by measuring the asymmetric momentum distribution of O$^+$ fragments produced from CO$_2{}^{2+}$ in two-color intense laser fields [34,35]. In the present experimental setup, the electric field has larger amplitudes on the positive side on the z axis with the relative phase $\phi = 0$, while the direction is reversed with $\phi = \pi$ (see inset of Fig. 2). Pulse durations of the fundamental and second harmonics after transmission through all optical components including the chamber window were measured to be 45 and 70 fs, respectively, by using the transient-grating frequency-resolved optical gating (TG-FROG) technique. The peak intensities of the fundamental and second harmonic fields, I_ω and $I_{2\omega}$, in the interaction region were estimated by the recoil ion momentum of H$_2{}^+$ [39].

The phase-locked two-color laser pulses were introduced into an ultrahigh-vacuum chamber and collinearly focused onto an effusive molecular beam of NO by a concave mirror ($f = 75$ mm). Ions produced in intense laser fields were accelerated by a homogeneous electric field of 61 V/cm to a position-sensitive detector (RoentDek HEX80) after a field-free region. The three-dimensional momentum vector of N$^+$ fragments, $\boldsymbol{p}_{\mathrm{N}^+} = (p_x, p_y, p_z)$, was calculated from position and arrival time at the detector for each dissociation event. The momentum vector of the neutral O fragments, $\boldsymbol{p}_\mathrm{O}$, produced as a counterpart of the N$^+$ fragments, was set to be equal to $-\boldsymbol{p}_{\mathrm{N}^+}$ by momentum conservation of the two heavy particles. Hence, the total kinetic energy release (KER) was calculated as

$$E_{\mathrm{kin}} = \frac{m_\mathrm{N} + m_\mathrm{O}}{2m_\mathrm{N}m_\mathrm{O}}|\boldsymbol{p}_{\mathrm{N}^+}|^2, \tag{4}$$

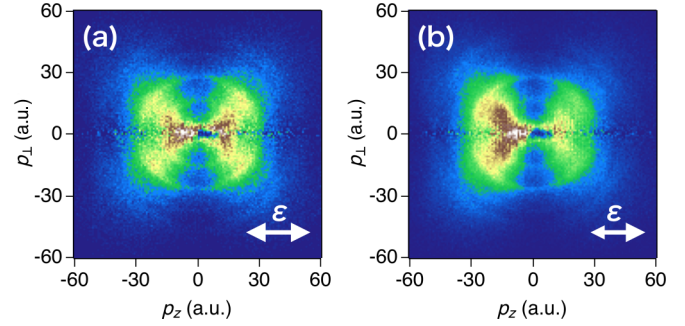where m_N and m_O are the masses of N and O atoms, respectively.

FIG. 3. Two-dimensional momentum images of the N$^+$ fragment ions produced in (a) one-color intense laser fields (800 nm, 1×10^{14} W/cm^2, 45 fs), (b) phase-locked two-color intense laser fields (800 nm + 400 nm, 1×10^{14} W/cm^2, 45 fs, $I_{2\omega}/I_\omega = 0.04$) with a relative phase of $\phi = 0.1\pi$. The momentum map represents a thin slice (with a slice width of ± 0.5 a.u.) of the three-dimensional momentum distribution in the plane containing the z axis (laser polarization direction). The momentum components parallel and perpendicular to the z axis are denoted with p_z and $p_\perp$, respectively. The laser polarization direction is denoted as ε with the arrow representing the direction of the larger amplitude.

III. RESULTS AND DISCUSSIONS

A. Ion momentum distributions

Figure 3(a) shows the two-dimensional momentum map obtained for the N$^+$ ions produced by the dissociative ionization of NO in NIR intense laser fields (45 fs, 800 nm, 1×10^{14} W/cm^2). The momentum map represents a thin slice (with a slice width of ± 0.5 a.u.) of the three-dimensional momentum distribution in the plane containing the z axis (laser polarization direction). The N$^+$ momentum image shows a butterflylike pattern, similar to that observed in the previous study [11] peaked at about $\theta = 40°$ and $140°$ with respect to the laser polarization direction. These angles reflect the shape of the 2π HOMO, because ionization proceeds efficiently when the laser electric field is applied along the orbital lobe in the molecular frame. The molecular dissociation subsequent to the tunneling ionization ejects the fragment ion with an offset angle against the laser polarization [11]. The significantly smaller ion yields at 0° and 90° correspond to the nodes of the 2π orbital. As in the previous study [11], the asymmetry of the MO is not observed in the ion image, due to the spatial symmetry of the laser electric fields.

Figure 3(b) shows the N$^+$ momentum image in two-color intense laser fields with the total intensity $I = I_\omega + I_{2\omega} = 1 \times 10^{14}$ W/cm^2 ($I_{2\omega}/I_\omega = 0.04$) and the relative phase $\phi = 0.1\pi$, where we observed the largest asymmetry [see Fig. 4(a)]. Compared with the ion image recorded with the fundamental laser fields in Fig. 3(a), the two-color field image shows larger yields on the left-hand side, while preserving the butterflylike pattern as obtained with the fundamental fields alone. To clarify the role of the two-color laser fields, we studied how the ion image varies by the relative phase ϕ. To quantitatively discuss the asymmetric fragmentation along the laser field, we define the asymmetry parameter,

$$A(\phi) = \frac{Y_\mathrm{R}(\phi) - Y_\mathrm{L}(\phi)}{Y_\mathrm{R}(\phi) + Y_\mathrm{L}(\phi)}, \tag{5}$$
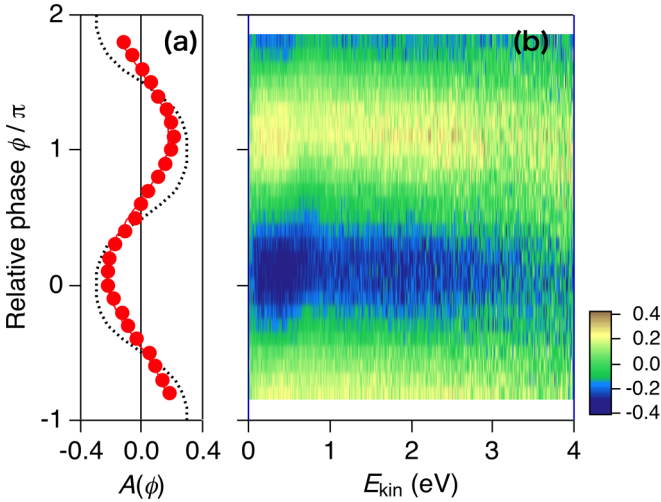
FIG. 4. (a) The asymmetry parameter $A(\phi)$ of the N^+ fragment ions in phase-locked two-color intense laser fields, integrated over the entire E_{kin} range ($0 \leqslant E_{kin} \leqslant 4$ eV) (solid circle). Theoretical asymmetry parameter calculated by ME-WFAT is plotted for comparison (dotted line). (b) Observed asymmetry parameter $A(\phi)$ plotted against the kinetic energy release E_{kin}.

where $Y_R(\phi)$ and $Y_L(\phi)$ are the yields of the N^+ fragments ejected in the hemispheres with positive ($p_z > 0$) and negative ($p_z < 0$) momenta along the laser polarization direction, respectively. The asymmetry parameter is plotted as a function of ϕ in Fig. 4(a). The obtained results show a clear oscillatory behavior with the amplitude of $|A| = 0.24$, where the minimum and maximum appear at $\phi \sim 0$ and π, respectively. The obtained results show that the N^+ fragments are preferentially ejected to the lower amplitude side of phase-locked two-color laser fields (see Fig. 2). The observed results suggest that the tunneling ionization occurs more efficiently from the N atom side, whose electron density is larger than that on the O atom side. The results are consistent with the previous experiments [30] on the directional dissociation of NO in the ω-2ω two-color laser fields carried out at higher field intensity (3×10^{14} W/cm^2), though the asymmetry amplitude for the dissociative ionization pathway is about one order smaller than that of the present results.

B. Kinetic energy release spectra

The ion images in Fig. 3 show that the momentum distribution consists of several radial components. These are also clearly visible in the KER spectrum in Fig. 5(a). The main peak is observed at 0.75 eV (peak II) in the KER spectrum, which is accompanied by three additional peaks (shoulders) at 0.3 (peak I), 1.3 (peak III), and 2.2 eV (peak IV). A similar spectrum is observed with the ω pulse alone as shown in the same figure.

The observed spectra are compared with the KER spectrum obtained using 8-fs intense laser fields (800 nm, 1.1×10^{14} W/cm^2) [11] [see dotted line in Fig. 5(a)], where two sharper peaks appear at 0.7 and 2.2 eV. Since these peaks are also observed in single-photon absorption experiments at $h\nu = 24$ eV [40], they are assigned to the dissociative ionization via the $c^3\Pi$ or $B^1\Pi$ dissociative states of NO^+
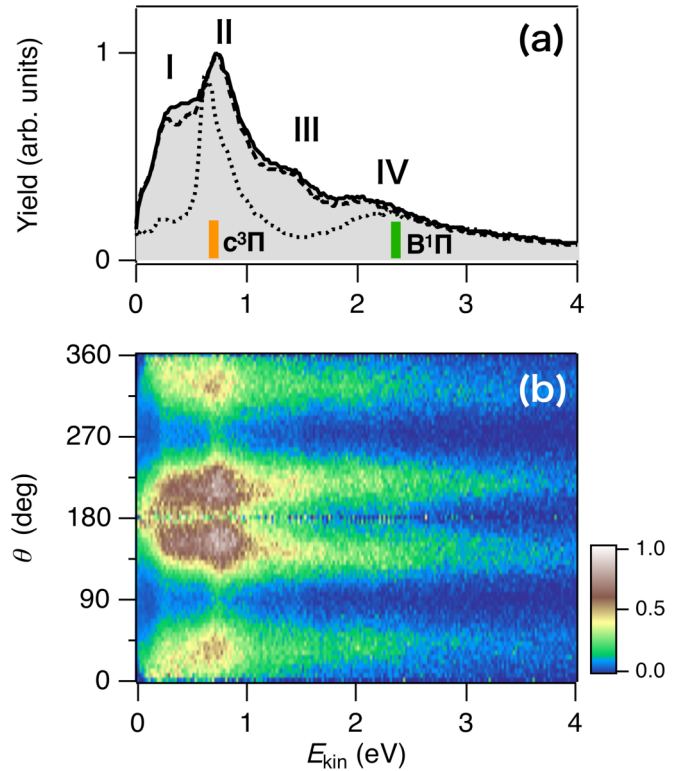

FIG. 5. (a) The total kinetic energy release, E_{kin}, spectra calculated by the momentum conservation from the N^+ fragment ions produced in two-color 45-fs intense laser fields $\phi = 0.1\pi$ (solid line), one-color 45-fs intense laser fields (broken line), and one-color 8-fs laser fields [11] (dotted line). (b) Two-dimensional plot of yields of the N^+ fragment ions produced in two-color intense laser fields (1×10^{14} W/cm^2, $I_{2\omega}/I_\omega = 0.04$, $\phi = 0.1\pi$) against the angle θ with respect to the laser polarization direction and E_{kin}.

from the Franck-Condon region of the neutral ground state (see Fig. 1). By using elliptically polarized intense laser fields, the previous study [11] showed that electron rescattering is responsible for populating the $c^3\Pi$ or $B^1\Pi$ dissociative states after tunneling ionization. Since the KER spectral profile of peak IV observed with the ω-2ω two-color laser fields remains essentially the same as in the 8-fs case, this component can be attributed to the rescattering excitation to the $B^1\Pi$ dissociative states of NO^+.

The broadened KER spectra observed in the present study suggest that additional pathways other than the direct excitation to the dissociative states contribute to the long laser pulse case (45 fs). Since the electron rescattering can also populate bound excited states of NO^+ near the dissociation threshold, the observed non-Franck-Condon dissociation could be attributed to the interaction between the bound NO^+ states and the remaining laser fields. The vibrational wave packets formed by electron rescattering should propagate toward their outer turning points of the bound potentials. Since the energy difference between the bound and repulsive states decreases as the internuclear distance increases, photodissociation from the bound state can proceed through a few-photon or single-photon coupling at large internuclear distances. In other words, the photoexcitation from the bound states favors dissociation at the large internuclear distances, explaining the

non-Franck-Condon dissociation pathways observed in the KER spectra in Fig. 5(a). It should be noted that this pathway is not open in few-cycle laser fields [11], since the pulse duration is too short for the bond stretching for the photodissociation at the large internuclear distances. The bound states can be populated directly by tunneling ionization from next HOMOs (HOMO-1 or HOMO-2) as discussed for other molecules such as CO [7,13], HCl [6], and O_2 [12]. In the present case, tunneling ionization from the 5σ orbital forms the excited bound states of NO^+, $A\,^1\Pi$, and $b\,^3\Pi$, while the $a\,^3\Sigma^+$, $w\,^3\Delta$, $W\,^1\Delta$, $b'\,^3\Sigma^-$, and $A'\,^1\Sigma^-$ states are formed by tunneling ionization from 1π orbitals [41] (see Fig. 1). Note that both the collisional excitation and the tunneling ionization to these excited states do not necessarily obey the dipole selection rules. The clear assignment of peaks I–III is not straightforward, due to many bound and dissociative states lying in the energy region near the dissociation limit (Fig. 1) [41,42]. A detailed theoretical study incorporating both the evolution of vibrational wave packets in strongly coupled electronic states [13] and the ionization to each bound state is necessary for a clear interpretation of the KER spectra in the lower-energy region.

C. Fragment angular distributions

In Fig. 5(b), the distribution of the N^+ yield in Fig. 3(b) is plotted as a function of E_{kin} and ejection angle θ measured from the z axis. The two-dimensional map exhibits clear stripes highlighted at four different angles of $\theta \sim$ 40°, 140°, 220°, and 320°, associated with the butterflylike shape in the ion image. A close inspection of the observed distribution reveals that the stripes gradually thin down, showing that the angular distributions depend on E_{kin}. The dependence is more apparent in Fig. 6, where the polar plots of the angular distributions are shown for the four peaks in the KER spectra, I, II, III, and IV. The fragment angular distribution has maxima at $\theta = 140°$ and 220° for peak IV, while peak I at 0.3 eV exhibits a broad distribution centered roughly at $\theta = 180°$.

The observed dependence on E_{kin} can be interpreted in terms of the photodissociating bound excited states of NO^+ discussed above. Since peak IV is associated with the direct rescattering excitation to the dissociative states via tunneling ionization from the 2π HOMO, the fragment angular distribution exhibits a clear butterflylike pattern. Since excitation to the repulsive states is involved for peaks I–III, the angle dependence of the transition moments additionally contributes to the fragment angular distribution [43,44]. If the parallel transition dominates the excitation, the fragment distribution is enhanced preferentially in the laser polarization direction. The angular dependence could be further modified if the transition probability depends on the orientation of the molecule in the asymmetric laser fields.

These bound states could be populated directly by tunneling ionization from next HOMOs 1π and 5σ instead of the rescattering excitation from the ground state of NO^+ as discussed in the previous section. In this case, the fragment angular distribution is expected to show angular distributions stretched along the laser polarization direction because these HOMOs have elongated shapes along the molecular axis as shown in Fig. 1(b). It is worth noting that the fragment
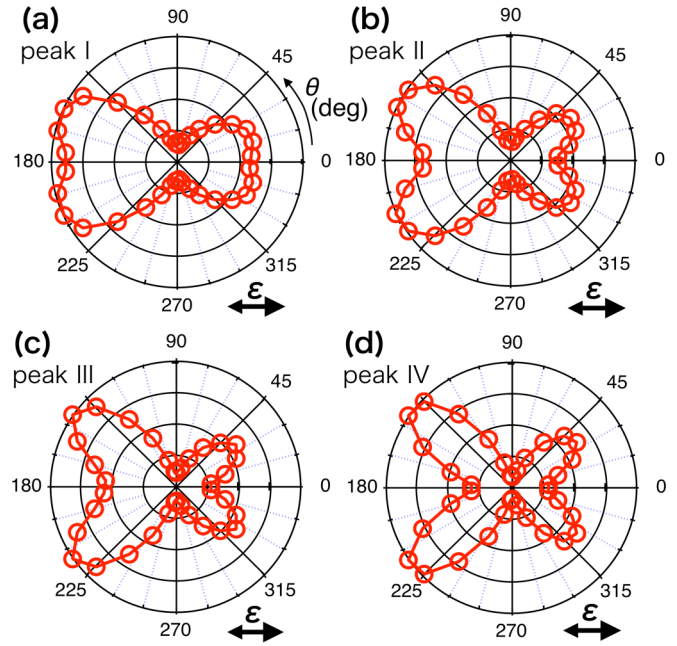

FIG. 6. Polar plot of θ angle distribution of the N^+ fragment ions produced by the dissociative ionization $NO \rightarrow N^+ + O + e^-$ in two-color intense laser fields. The relative phase of $\phi = 0.1\pi$. (a) Peak I ($0.14 \leqslant E_{kin} \leqslant 0.36$ eV), (b) peak II ($0.50 \leqslant E_{kin} \leqslant 1.0$ eV), (c) peak III ($1.2 \leqslant E_{kin} \leqslant 1.7$ eV), and (d) peak IV ($1.8 \leqslant E_{kin} \leqslant 4.0$ eV). The laser polarization direction is denoted as ε with the larger arrow representing the direction of the larger amplitude.

asymmetry parameter shows a similar dependence on the relative phase over the entire range of KER as shown in Fig. 4(b). Since the highest KER peak IV is attributed to the direct rescattering process from 2π HOMO, this phase dependence may indicate that the rescattering excitation to the bound states is more significant than the tunneling ionization from HOMO-1 and HOMO-2 for peaks I–III.

D. Comparison with tunneling ionization theory

Here the angular distribution of peak IV, the direct rescattering pathway, is compared with theoretical calculations of tunneling ionization from the 2π HOMO. According to ME-WFAT [19], which can naturally incorporate the effect of the dipole moment, the tunneling ionization rate for the field strength F at the molecular orientation angle with respect to the polarization axis β is expressed as

$$\Gamma(\beta, F) = \left\{ |G_{00}(\beta)|^2 + \frac{F}{2\varkappa^2} \left[|G_{01}^{(+)}(\beta)|^2 + |G_{01}^{(-)}(\beta)|^2 \right] \right\}$$
$$\times W_{00}(F). \qquad (6)$$

Here $W_{00}(F)$ is the field factor which is explicitly expressed as

$$W_{00}(F) = \frac{\varkappa}{2} \left(\frac{4\varkappa^2}{F} \right)^{2/\varkappa - 1} \exp\left(-\frac{2\varkappa^3}{3F} \right), \qquad (7)$$

and $\varkappa = \sqrt{2I_p}$ with I_p being the ionization potential given by the energy difference between the NO and NO^+ states.
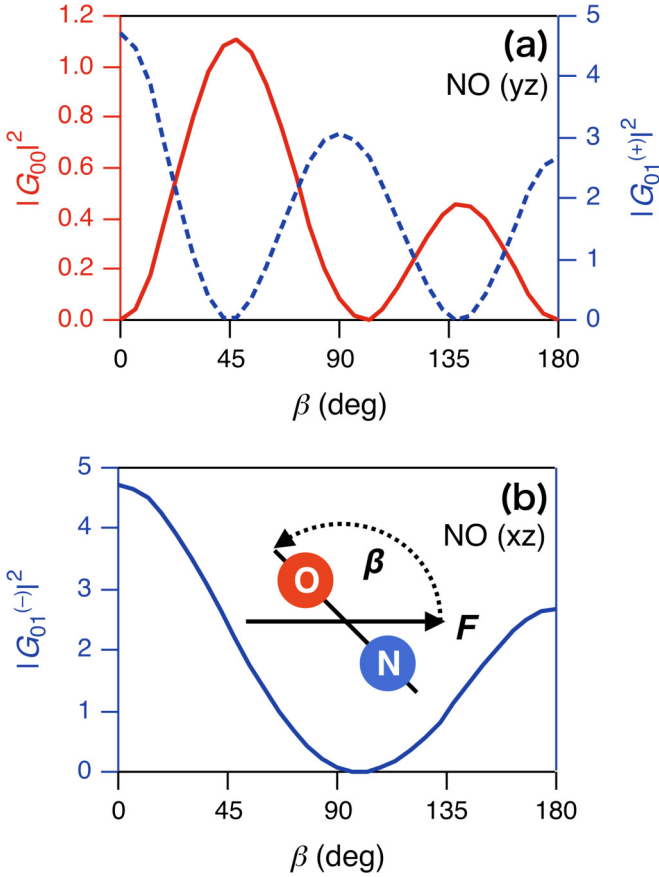
FIG. 7. Structure factors of NO plotted against orientation angle β between the electric field and the molecular axis. (a) $|G_{00}(\beta)|^2$ (solid line) and $|G_{01}^{(+)}(\beta)|^2$ (dashed line) for $2\pi(yz)$ HOMO and (b) $|G_{01}^{(-)}(\beta)|^2$ for $2\pi(xz)$ HOMO.

$G_{0m}^{(\pm)}(\beta)$ ($m = 0, 1$) is the structure factor [18,45] given by

$$G_{0m}^{\pm}(\beta) = e^{-\mu \cos \beta} g_{0m}^{(\pm)}(\beta), \qquad (8)$$

where μ is the dipole moment difference between the NO and NO$^+$ ground states along the molecular axis pointing from the N to O atoms, and $g_{0m}(\beta)$ is the asymptotic coefficient determined by the expansion of the Dyson orbital in terms of the parabolic basis. The superscripts ($\pm$) denote the two degenerated orbitals, (+) for the $2\pi(xz)$ state and (−) for the $2\pi(yz)$ state (see Ref. [38]), and we assume that they are equally distributed in the experiments. Note that the β dependence is only in the structure factors in the WFAT.

To implement the ME-WFAT, we calculate the energy difference and the dipole difference within the Hartree-Fock (HF) approximation using the X2DHF code [46]. In the present case, $I_p = 0.41$ a.u. and $\mu = 0.26$ a.u. at the geometrical center, pointing from N to O. To calculate the structure coefficients, we use the HF 2π HOMO in place of the corresponding Dyson orbital, which is a good approximation for small diatomic molecules. The resulting structure factors are shown in Fig. 7. To compare with the experimental results, we assume that the angular distribution of N$^+$ fragments at peak IV, $S(\theta)$, is proportional to the tunneling ionization yield. The yield is obtained by the time integration of the tunneling rate
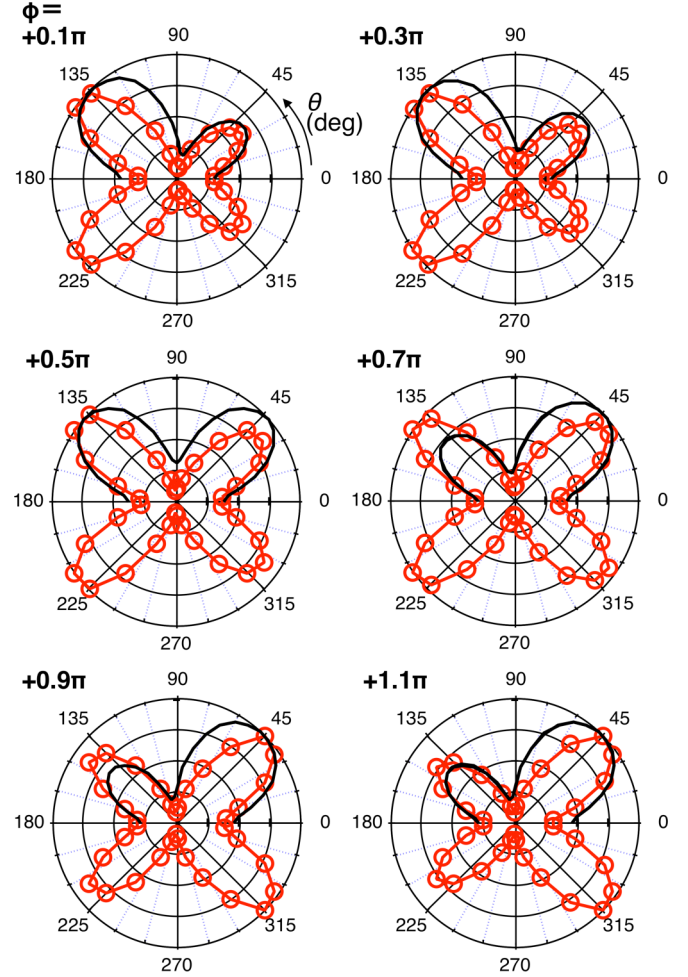

FIG. 8. Dependence of the angular distribution of peak IV on the relative phase ϕ. The laser polarization direction is along the horizontal axis. Experimental results show clear dependence on the phase (open circle). Theoretical results obtained by ME-WFAT (1×10^{14} W/cm^2) are shown in the first and second quadrants (solid line) for comparison.

in Eq. (6) over the two-color laser pulse at a given molecular orientation to the laser electric fields, i.e.,

$$S(\theta) \propto 1 - \exp\left[-\int_{-\infty}^{+\infty} \Gamma(\beta, F(t)) dt \right], \qquad (9)$$

where $\beta = \pi - \theta$ for $F(t) \geqslant 0$ and $\beta = \theta$ for $F(t) < 0$. In the time integration, the Gaussian functions are assumed for the envelopes, $\bar{F}_\omega(t)$ and $\bar{F}_{2\omega}(t)$ in Eq. (3).

The theoretical results are compared with the experimental data recorded at different phases in Fig. 8. At $\phi = 0.1\pi$, the theoretical result exhibits a clear butterflylike structure with the larger peak at $\sim 135°$ and the smaller peak at $\sim 45°$. This shows that the ionization proceeds preferentially on the smaller amplitude side of the ω-2ω laser electric fields [30], in good agreement with the experimental result. The theoretical calculation reproduces the phase dependence of the angular distribution, which shows gradual variation of the asymmetry along the laser polarization direction, with the peak angles remaining essentially the same.

Let us discuss the effect of the dipole moment in the orientation dependence of the ionization rate. Due to the positive value of the dipole difference μ in the exponential factor in Eq. (8), the structure factor and thus the ionization rate are suppressed when the NO molecule is oriented along the field ($\beta < 90°$); i.e., less ionization from the N atom side is expected. On the other hand, the dominant structure coefficient $g_{00}(\beta)$ in Eq. (8) is larger for the same orientation due to a larger electron density for the N atom side. As a result of the product of the two terms, the structure factor and thus the ionization rate show that the shape of the molecular orbital in the structure coefficient governs the tunneling ionization of NO. The obtained result shows a clear contrast to the case of CO. In the latter, the WFAT within the HF approximation predicted that tunneling ionization occurs more preferentially from the O atom side due to a positive value of the dipole of HOMO, pointing from the C to the O atoms, in the exponential factor [38]. However, the experimental results indicate that tunneling ionization from the C atom side is predominant [7,33].

The asymmetry parameter calculated from the tunneling ionization yields shows a clear dependence on the relative phase ϕ as shown in Fig. 4(a). The largest asymmetry is obtained at $\phi = 0$ and π, which agrees with the experimental results except for a small phase shift (0.1 π). The shift is also seen in the phase dependence of the angular distribution in Fig. 8. In addition, the experimental angular distribution shows narrower widths with peak angles slightly shifted toward the polarization axis. These deviations could be attributed to the multiorbital effects [23,28] discussed to explain the angular distributions of the tunneling ionization of CO. In addition, the electron rescattering involved in the dissociation process could also contribute. Since the molecular potential of NO$^+$ is anisotropic, the cross section of electron impact excitation, NO$^+$ + e^- → N$^+$ + O + e^-, is expected to vary with the orientation of the molecular ion, which results in the modification of the angular distribution of the fragment ions. It is worth noting that the electron rescattering energy depends on the relative phase of the two-color laser fields [35]. In particular, the maximum rescattering energy increases as the relative phase increases from $\phi \sim 0$. This indicates that the rescattering excitation to the excited states of NO$^+$ is more efficient for a positive phase than $\phi = 0$, which may result

in the shift of the peak phase from the theoretical prediction in Fig. 4(a). For a deeper understanding, theoretical studies incorporating electron rescattering excitation would be useful.

IV. SUMMARY

We have investigated the angle dependence of dissociative tunneling ionization of NO, NO → N$^+$ + O + e^-, in asymmetric two-color intense laser fields (45 fs, 1×10^{14} W/cm^2) by three-dimensional ion-momentum imaging of N$^+$ fragment. The N$^+$ fragment ion with the highest kinetic energy release ($\geqslant 1.8$ eV) produced by electron rescattering excitation after the tunneling ionization to the NO$^+$ $X\,^1\Sigma^+$ state shows an angular distribution peaked at 40° with respect to the laser polarization direction. A clear asymmetry observed in the ion image shows that the tunneling ionization occurs efficiently when the electric field points from N to O. The orientation dependence agrees with the theoretical prediction for tunneling ionization from the 2π orbital of NO by ME-WFAT, showing that the shape of the molecular orbital in the structure factor governs the tunneling ionization of NO. On the other hand, the N$^+$ angular distribution shows a clear dependence on the kinetic energy release, where peak angles shift toward the laser polarization direction as the kinetic energy release decreases. This dependence is interpreted as a result of photodissociation from bound excited states of NO$^+$, which are populated by tunneling ionization from next highest occupied molecular orbitals or by electron rescattering.

[1] C. D. Lin, A.-T. Le, Z. Chen, T. Morishita, and R. Lucchese, J. Phys. B **43**, 122001 (2010).

[2] J. Xu, C. I. Blaga, P. Agostini, and L. F. DiMauro, J. Phys. B **49**, 112001 (2016).

[3] L. Holmegaard, J. L. Hansen, L. Kalhøj, S. L. Kragh, H. Stapelfeldt, F. Filsinger, J. Küpper, G. Meijer, D. Dimitrovski, M. Abu-samha, C. P. J. Martiny, and L. Bojer Madsen, Nat. Phys. **6**, 428 (2010).

[4] J. L. Hansen, L. Holmegaard, J. H. Nielsen, H. Stapelfeldt, D. Dimitrovski, and L. B. Madsen, J. Phys. B **45**, 015101 (2012).

[5] A. Staudte, S. Patchkovskii, D. Pavicic, H. Akagi, O. Smirnova, D. Zeidler, M. Meckel, D. M. Villeneuve, R. Dörner, M. Y. Ivanov, and P. B. Corkum, Phys. Rev. Lett. **102**, 033004 (2009).

[6] H. Akagi, T. Otobe, A. Staudte, A. Shiner, F. Turner, R. Dörner, D. M. Villeneuve, and P. B. Corkum, Science **325**, 1364 (2009).

[7] J. Wu, L. P. H. Schmidt, M. Kunitski, M. Meckel, S. Voss, H. Sann, H. Kim, T. Jahnke, A. Czasch, and R. Dörner, Phys. Rev. Lett. **108**, 183001 (2012).

[8] M. Magrakvelidze, F. He, S. De, I. Bocharova, D. Ray, U. Thumm, and I. V. Litvinyuk, Phys. Rev. A **79**, 033408 (2009).

[9] A. S. Alnaser, S. Voss, X. M. Tong, C. M. Maharjan, P. Ranitovic, B. Ulrich, T. Osipov, B. Shan, Z. Chang, and C. L. Cocke, Phys. Rev. Lett. **93**, 113003 (2004).

[10] A. S. Alnaser, C. M. Maharjan, X. M. Tong, B. Ulrich, P. Ranitovic, B. Shan, Z. Chang, C. D. Lin, C. L. Cocke, and I. V. Litvinyuk, Phys. Rev. A **71**, 031403(R) (2005).

[11] T. Endo, A. Matsuda, M. Fushitani, T. Yasuike, O. I. Tolstikhin, T. Morishita, and A. Hishikawa, Phys. Rev. Lett. **116**, 163002 (2016).

[12] H. Liu, S.-F. Zhao, M. Li, Y. Deng, C. Wu, X.-X. Zhou, Q. Gong, and Y. Liu, Phys. Rev. A **88**, 061401(R) (2013).

[13] I. Znakovskaya, P. von den Hoff, S. Zherebtsov, A. Wirth, O. Herrwerth, M. J. J. Vrakking, R. de Vivie-Riedle, and M. F. Kling, Phys. Rev. Lett. **103**, 103002 (2009).

[14] D. Pavicic, K. F. Lee, D. M. Rayner, P. B. Corkum, and D. M. Villeneuve, Phys. Rev. Lett. **98**, 243001 (2007).

[15] X. M. Tong, Z. X. Zhao, and C. D. Lin, Phys. Rev. A **66**, 033402 (2002).

[16] J. Muth-Bohm, A. Becker, and F. H. M. Faisal, Phys. Rev. Lett. **85**, 2280 (2000).

[17] D. Dimitrovski, C. P. J. Martiny, and L. B. Madsen, Phys. Rev. A **82**, 053404 (2010).

[18] O. I. Tolstikhin, T. Morishita, and L. B. Madsen, Phys. Rev. A **84**, 053423 (2011).

[19] O. I. Tolstikhin, L. B. Madsen, and T. Morishita, Phys. Rev. A **89**, 013421 (2014).

[20] S. Petretti, Y. V. Vanne, A. Saenz, A. Castro, and P. Decleva, Phys. Rev. Lett. **104**, 223001 (2010).

[21] T. Otobe, K. Yabana, and J.-I. Iwata, Phys. Rev. A **69**, 053404 (2004).

[22] B. Zhang, J. Yuan, and Z. Zhao, Phys. Rev. Lett. **111**, 163001 (2013).

[23] S. Ohmura, T. Kato, T. Oyamada, S. Koseki, H. Ohmura, and H. Kono, J. Phys. B **51**, 034001 (2018).

[24] M. Abu-samha and L. B. Madsen, Phys. Rev. A **80**, 023401 (2009).

[25] R. Murray, M. Spanner, S. Patchkovskii, and M. Y. Ivanov, Phys. Rev. Lett. **106**, 173001 (2011).

[26] M. D. Śpiewanowski and L. B. Madsen, Phys. Rev. A **91**, 043406 (2015).

[27] H. Akagi, T. Otobe, and R. Itakura, Sci. Adv. **5**, eaaw1885 (2019).

[28] V. P. Majety and A. Scrinzi, J. Phys. B **48**, 245603 (2015).

[29] A. Iwamae, A. Hishikawa, and K. Yamanouchi, J. Phys. B **33**, 223 (2000).

[30] H. Li, D. Ray, S. De, I. Znakovskaya, W. Cao, G. Laurent, Z. Wang, M. F. Kling, A. T. Le, and C. L. Cocke, Phys. Rev. A **84**, 043429 (2011).

[31] W. Hu, Y. Liu, S. Luo, X. Li, J. Yu, X. Li, Z. Sun, K.-J. Yuan, A. D. Bandrauk, and D. Ding, Phys. Rev. A **99**, 011402(R) (2019).

[32] Y. Liu, W. Hu, S. Luo, K.-J. Yuan, Z. Sun, A. D. Bandrauk, and D. Ding, Phys. Rev. A **100**, 023404 (2019).

[33] H. Ohmura, N. Saito, and T. Morishita, Phys. Rev. A **89**, 013405 (2014).

[34] T. Endo, H. Fujise, A. Matsuda, M. Fushitani, H. Kono, and A. Hishikawa, J. Electron Spectrosc. Relat. Phenom. **207**, 50 (2016).

[35] T. Endo, H. Fujise, Y. Kawachi, A. Ishihara, A. Matsuda, M. Fushitani, H. Kono, and A. Hishikawa, Phys. Chem. Chem. Phys. **19**, 3550 (2017).

[36] D. Ray, F. He, S. De, W. Cao, H. Mashiko, P. Ranitovic, K. P. Singh, I. Znakovskaya, U. Thumm, G. G. Paulus, M. F. Kling, I. V. Litvinyuk, and C. L. Cocke, Phys. Rev. Lett. **103**, 223201 (2009).

[37] I. Y. Tolstikhina, T. Morishita, and O. I. Tolstikhin, Phys. Rev. A **90**, 053413 (2014).

[38] R. Saito, O. I. Tolstikhin, L. B. Madsen, and T. Morishita, At. Data Nucl. Data Tables **103**, 4 (2015).

[39] A. S. Alnaser, X. M. Tong, T. Osipov, S. Voss, C. M. Maharjan, B. Shan, Z. Chang, and C. L. Cocke, Phys. Rev. A **70**, 023413 (2004).

[40] A. Lafosse, M. Lebech, J. C. Brenot, P. M. Guyon, O. Jagutzki, L. Spielberger, M. Vervloet, J. C. Houver, and D. Dowek, Phys. Rev. Lett. **84**, 5987 (2000).

[41] D. L. Albritton, A. L. Schmeltekopf, and R. N. Zare, J. Chem. Phys. **71**, 3271 (1979).

[42] H. Partridge, S. R. Langhoff, and C. W. Bauschlicher, J. Chem. Phys. **93**, 7179 (1990).

[43] A. Hishikawa, S. L. Liu, A. Iwasaki, and K. Yamanouchi, J. Phys. Chem. **114**, 9856 (2001).

[44] A. M. Sayler, P. Q. Wang, K. D. Carnes, B. D. Esry, and I. Ben-Itzhak, Phys. Rev. A **75**, 063420 (2007).

[45] L. B. Madsen, O. I. Tolstikhin, and T. Morishita, Phys. Rev. A **85**, 053404 (2012).

[46] J. Kobus, L. Laaksonen, and D. Sundholm, Comput. Phys. Commun. **98**, 346 (1996).